Polarization-Insensitive Nano-Metamaterial Sensor With Near-Infrared μ and ε Negative Properties for Early Cancer Detection via Exosome Analysis (70 THz to 3 PHz)

Musa N. Hamza, Mohammad Tariqul Islam, *Senior Member, IEEE*, Sunil Lavadiya, Iftikhar ud Din, Bruno Sanches, Slawomir Koziel, Syeda Iffat Naqvi, *Senior Member, IEEE*, Abinash Panda, *Member, IEEE*, Mohammad Alibakhshikenari, *Member, IEEE*, B. Virdee, *Senior Member, IEEE*, and Md. Shabiul Islam, *Senior Member, IEEE*

***Abstract*—Metamaterials (MTMs) have emerged as essential components in high-performance electromagnetic devices, including sensors and absorbers. This study presents a polarization-insensitive nano-metamaterial sensor with exceptional angular stability and a wide operating range of 70 THz to 3 PHz. The sensor achieves an average absorption rate of 97% across this range, making it highly suitable for applications in biomedical engineering. By integrating microwave imaging (MWI) techniques, the sensor can detect circulating cancer exosomes (CCEs) with high sensitivity, effectively distinguishing them from normal exosomes. Exhibiting double-negative MTM properties (negative permittivity and permeability) in the near-infrared (NIR) range (70 THz to 400 THz), the sensor enhances sensitivity for early cancer detection. A detailed analysis of its properties, including impedance (Z), phase, and S_{11} parameters (real and imaginary components), demonstrates its superior performance. This non-invasive, label-free approach to detecting cancer biomarkers represents a significant step forward in advancing personalized healthcare.**

***Index Terms*—Nano-metamaterial sensor, DNG MTMs NIR sensor, exosome-based diagnostics, early-stage cancer diagnostics, microwave imaging techniques.**

Received 26 January 2025; accepted 3 March 2025. Date of publication 11 March 2025; date of current version 2 April 2025. This work was supported in part by the University of Doha for Science and Technology under Grant KK-2024-005, in part by Icelandic Research Fund under Grant 239858, and in part by the National Science Centre of Poland under Grant 2020/37/B/ST7/01448. *(Corresponding authors: Musa N. Hamza; Mohammad Tariqul Islam; Mohammad Alibakhshikenari; Md. Shabiul Islam.)*

Musa N. Hamza is with the Department of Physics, College of Science, University of Raparin, Sulaymaniyah 46012, Iraq (e-mail: musa.nuraden@uor.edu.krd).

Mohammad Tariqul Islam is with the Department of Electrical, Electronic and Systems Engineering, Faculty of Engineering and Built Environment, Universiti Kebangsaan Malaysia, Bangi, Selangor 43600, Malaysia (e-mail: tariqul@ukm.edu.my).

Sunil Lavadiya is with the Department of Information and Communication Technology, Marwadi University, Rajkot, Gujarat 360003, India (e-mail: sunil.lavadiya@marwadieducation.edu.in).

Iftikhar ud Din is with the Telecommunication Engineering Department, University of Engineering and Technology, Mardan 23200, Pakistan (e-mail: iftikharuddin114@gmail.com).

Bruno Sanches is with the Department of Electronic Systems Engineering, Escola Politécnica da Universidade de São Paulo São Paulo, São Paulo 05508-010, Brazil (e-mail: bruno.csanches@usp.br).

Slawomir Koziel is with the Engineering Optimization & Modeling Center, Reykjavik University, 102 Reykjavik, Iceland, and also with the Faculty of Electronics, Telecommunications and Informatics, Gdansk University of Technology, 80-233 Gdansk, Poland (e-mail: koziel@ru.is).

Syeda Iffat Naqvi is with the Department of Telecommunication Engineering, University of Engineering & Technology Taxila, Taxila 47050, Pakistan (e-mail: iffat.naqvi@uettaxila.edu.pk).

Abinash Panda is with the Department of Electronics and Communication Engineering, CMR Institute of Technology, Bengaluru 560037, India (e-mail: abinashpanda087@gmail.com).

Mohammad Alibakhshikenari is with the Electronics Engineering Department, University of Rome "Tor Vergata", 00133 Rome, Italy (e-mail: alibakhshikenari@ing.uniroma2.it).

B. Virdee is with the Department of Center for Communications Technology, London Metropolitan University, N7 8DB London, U.K. (e-mail: b.virdee@londonmet.ac.uk).

Md. Shabiul Islam is with the Faculty of Engineering (FOE), Multimedia University (MMU), Cyberjaya, Selangor 63100, Malaysia (e-mail: shabiul.islam@mmu.edu.my).

Digital Object Identifier 10.1109/JPHOT.2025.3549946

I. Introduction

METAMATERIALS (MTMs) have garnered significant attention due to their extraordinary electromagnetic properties, particularly across microwave, infrared, and optical frequency ranges [1]. These engineered materials exhibit unconventional traits such as negative permittivity, negative permeability, and even a negative refractive index, which are not typically observed in natural materials. The theoretical concept of a negative refractive index was first introduced by V.G. Veselago in 1968 [2], laying the foundation for the development of MTMs. Unlike conventional materials, where electromagnetic properties depend on composition, the unique characteristics of metamaterials are derived from their engineered structures or constituent materials [3]. This versatility has enabled a broad spectrum of applications, including perfect lenses [4], chiral scanning [3], optical cloaking [5], antennas [6], filters [7], holograms [8], thermal imaging [9], sensors [10], and absorbers [11]. Metamaterials have also been instrumental in advancing GHz, THz, and low-PHz biosensors [12], [13], [14], [15], [16], [17], [18], [19], [20], [21], [22], [23], [24], [25], [26], [27], [28], [29], [30], [31], [32], [33], [34], [35], [36], [37], driving innovation in areas ranging from telecommunications to biomedical imaging [38], [39], [40].

Meta-surface-based absorbers represent a particularly compelling application of metamaterials. The concept was pioneered by Landy et al. in 2008 [41], showcasing highly engineered absorbers with unprecedented performance. Since then, numerous MTM sensors and absorbers have been developed across electromagnetic wavebands, including microwave, terahertz, and optical frequencies. These absorbers exhibit diverse functionalities, such as narrowband, broadband, polarization-sensitive, and polarization-insensitive designs, tailored for specific applications [42], [43], [44], [45], [46], [47], [48], [49], [50], [51]. Notably, the absorption spectrum of these devices can be significantly enhanced by incorporating nanostructured metamaterials. A widely used approach involves a three-layer metal-insulator-metal (MIM) configuration, where the top metal layer acts as a resonator, the ground metal layer absorbs electromagnetic waves, and the intermediate dielectric layer establishes coupling capacitance to boost performance [52].

Recent advancements in metamaterials have extended their operational range into the infrared and visible frequencies [53]. A key focus in nanostructured metamaterial research is to achieve wideband absorption with near-unity efficiency while maintaining compactness and angular stability. For instance, polarization-insensitive nanostructures made of Ni and SiO_2 demonstrate absorption efficiencies of 95%, 91%, and 93% with bandwidths of 1.29, 0.81, and 0.64 PHz, respectively [54], [55], [56]. Similarly, W and SiO_2-based absorbers with 92% absorption and a 0.63 PHz bandwidth have been proposed [57]. Other designs incorporating W, Al_2O_3, and Ti layers achieve absorption rates of 94% with a 0.44 PHz bandwidth, leveraging surface plasmon resonance (SPR) and localized surface plasmon resonance (LSPR) effects [58]. Polarization-sensitive absorbers have also been developed, achieving 92% and 97% absorption with bandwidths of 0.35 and 0.17 PHz, respectively [62], [63].

Cancer remains a leading cause of global morbidity and mortality, and early detection is crucial for improving outcomes. Current detection methods, such as MRI, PET, CT, and histopathology, often suffer from limited sensitivity and specificity, reducing their clinical effectiveness [64], [65], [66], [67], [68], [69], [70], [71]. Exosomes, a type of extracellular vesicle (EV), have emerged as promising biomarkers due to their role in cancer progression. Once considered cellular debris, EVs are now recognized for transferring bioactive molecules (proteins, lipids, DNA, RNA, and microRNA) to recipient cells, influencing cancer metastasis, drug resistance, and immune evasion [66], [67]. Their presence in bodily fluids like blood and urine makes exosomes ideal candidates for non-invasive diagnostics [72].

The NIR frequency range (70 THz–400 THz) bridges electronics and photonics, offering unique advantages for safe, non-invasive imaging of soft tissues. Techniques such as terahertz (THz) imaging enable high-resolution visualization of tissue structure and hydration, making them valuable for cancer diagnostics and other medical applications [73]. Metamaterial perfect absorbers (MTMPAs) in the THz range provide a cutting-edge approach for real-time, label-free detection of cancer-related exosomes. These absorbers can trap light at specific wavelengths, enabling sensitive detection of exosomes without the need for labeling, unlike conventional methods like ELISA [74], [75], [76], [77]. This real-time monitoring capability, even at low exosome concentrations, is critical for early cancer detection [78].

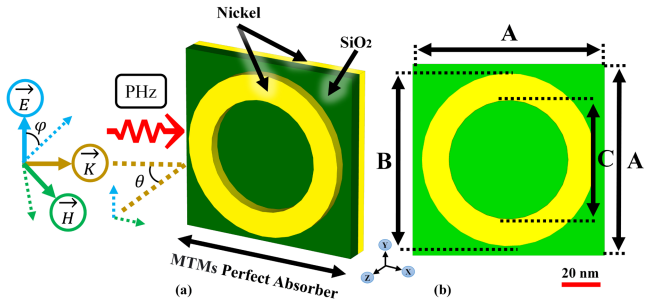

Fig. 1. Structural design and incident field orientations of a recommended perfect absorber; (a) schematic representation of the structural design and incident field orientations of a perfect absorber, and (b) proposed design model.

Developing a compact, ultra-thin absorber for infrared and visible light with strong polarization and angular stability is essential for real-time applications. This study introduces a polarization-insensitive nano-metamaterial absorber with high angular stability and a broad operating range from 70 THz to 3 PHz, achieving an impressive average absorption rate of 97%. To illustrate its versatility, the spectrum is divided into subranges, each suited for distinct applications. In the near-infrared (NIR) region (70 THz–400 THz), the sensor supports non-invasive imaging techniques such as optical coherence tomography (OCT) and near-infrared spectroscopy, both critical for early cancer detection. In the visible spectrum (400 THz–770 THz), it enables high-resolution imaging to identify cancer biomarkers. Moving into the ultraviolet (UV) range (770 THz–1.5 PHz), the absorber facilitates detailed molecular diagnostics, including DNA and protein analysis. Furthermore, in the far-UV region (1.5 PHz–3 PHz), it provides precise molecular fingerprinting capabilities for studying cancer-related biomolecular changes.

The proposed sensor also integrates microwave imaging (MWI) techniques to effectively detect circulating cancer exosomes (CCEs) with high sensitivity, distinguishing them from normal exosomes. In the NIR range, its double-negative properties further enhance sensitivity, making it particularly effective for early cancer detection. A comprehensive analysis of impedance, phase, and reflection coefficient (S_{11}) parameters underscores the sensor's potential as a non-invasive, label-free tool for identifying cancer biomarkers. These advancements position the sensor as a groundbreaking innovation in biomedical engineering and personalized healthcare.

II. Structural Design and Incident Field Orientations

This section discusses the key components of the proposed metamaterial perfect absorber, as illustrated in Fig. 1. The design follows the Metal-Insulator-Metal (MIM) configuration, utilizing sub-micrometer-sized structures placed on a fully developed metallic backplane. The silicon dioxide (SiO_2) layer, serving as the insulator, has a relative permittivity of 3.9 and a loss tangent of 10^{-4}, ensuring low optical losses and high performance in the absorber design.

TABLE I
A COMPLETE LIST OF THE VARIABLES THAT HAVE BEEN ADJUSTED FOR THE RECOMMENDED PERFECT MTMS ABSORBER

Parameter	Value (nm)	Parameter	Value (nm)
A	100	SiO_2 Thick	14
B	90	Ni Thick	6
C	62		

The selection of a circular ring structure with a median diameter of 76 nm was investigated for its suitability in the frequency range from 0 to 3 PHz to accommodate the first four modes. Circular ring-shaped structures are particularly well-suited for studying surface plasmon polaritons (SPPs) and resonance effects due to their symmetrical geometry and uniform field distribution, which facilitate efficient electromagnetic coupling with SPP modes. Additionally, the polarization-independent optical properties of this structure reduce edge effects and enhance inter-element coupling, making it highly effective for nanophotonic applications [79].

The chosen size allows for strong electromagnetic wave confinement and supports localized surface plasmon resonance (LSPR), resulting in enhanced field intensities and energy transfer [80]. Furthermore, this design is compatible with advanced nanofabrication techniques, enabling practical manufacturability. The covered frequency range, spanning the ultraviolet, visible, and near-infrared spectra, is crucial for applications such as plasmonic sensing, where sensitivity to environmental changes is critical, and spectroscopy, where enhanced field strength improves detection efficiency. The compact size of the structure facilitates integration into nanophotonic circuits, providing a robust platform for advancing nanophotonic technologies and enabling cutting-edge optical innovations [81].

Several material options were considered during the design process. For the insulator, silicon and titanium dioxide were evaluated, with silicon dioxide ultimately selected due to its superior properties. For the conductive components, nickel, silver, and gold were analysed. Nickel was chosen as the conductive material because it met the wideband requirements, ensured compatibility with the fabrication process, and offered cost-effectiveness.

A variety of structural configurations were reviewed, and the proposed solution was based on a streamlined approach utilizing a single-ring structure. Fig. 1 illustrates the primary geometric aspects of the designed perfect absorber and its orientation with respect to the reference fields and incident angles used in this study.

The metal resonator ring features an inner diameter of 62 nm, an outer diameter of 90 nm, and is constructed on a thin silicon dioxide layer with an average thickness of 14 nm. Table I summarizes the dimensions of the final design, which was optimized to maximize absorption while minimizing reflection and transmission across a wide frequency band extending up to 3 PHz.

The perfect absorber was designed using an industry-standard electromagnetic simulation suite and thoroughly evaluated. The next section presents the main results and absorption spectra obtained for the proposed metamaterial device.

Fig. 1 illustrates the structural setup and field orientation of the nano-metamaterial perfect absorber, designed to operate within the 70 THz to 3 PHz frequency range. High-frequency characterization in this range poses challenges due to the limitations of traditional electronic measurement techniques, which are inadequate beyond 70 THz. However, alternative optical methods, such as petahertz time-domain spectroscopy (PHz-TDS), LTEM, and thermal/pyroelectric techniques, provide feasible solutions for performance measurement and analysis.

The metamaterial structure consists of a patterned nickel layer on a SiO_2 substrate, optimized for efficient absorption of incident electromagnetic waves. The resonator design features a single-ring nickel structure, which addresses nanoscale fabrication challenges while enhancing manufacturability and sensor sensitivity. This single-ring setup also facilitates compatibility with exosome analysis, a key technique for early cancer detection. Electromagnetic interactions with the absorber, represented by the red arrow, occur at specific angles (θ and φ), with directional indicators for the electric field (E), magnetic field (H), and propagation vector (k) provided for assessing absorption effectiveness, as shown in Fig. 1(a).

The simulation of the nanoscale petahertz (PHz) metamaterial absorber was performed using CST Studio Suite, a high-fidelity electromagnetic simulation tool designed for modelling materials at sub-wavelength scales. To mitigate spurious reflections and ensure accurate absorption characteristics, Perfectly Matched Layers (PMLs) were applied as boundary conditions. These layers effectively absorbed outgoing waves, while the simulation domain was made sufficiently large to minimize near-field boundary effects. A refined mesh was used, especially around the intricate features of the metamaterial structure, to capture the fine details of electromagnetic interactions at the nanoscale.

To characterize the absorption properties across the operating frequency range of 70 THz to 3 PHz, plane wave sources served as the primary excitation method. These sources were carefully aligned with the polarization of the metamaterial to ensure uniform illumination. Additionally, port sources were utilized for specific simulations requiring directional excitation. Wave source parameters, including frequency and polarization, were chosen to match the resonant frequencies of the metamaterial, enabling highly accurate simulation results.

Post-processing techniques were crucial for evaluating the absorber's performance. Key parameters such as the absorption spectra, S-parameters (S_{11}), and electric field distributions were analysed to gain insights into the metamaterial's electromagnetic behaviour. These analyses confirmed the absorber's high absorption efficiency and sensitivity, making it highly suitable for applications in non-invasive biosensing technologies. This simulation methodology enabled the optimization of the metamaterial sensor, ensuring its capability to perform effectively in real-world applications such as early-stage cancer detection.

By adjusting parameters such as geometry (Fig. 1(b)) and the dielectric and metallic properties, the metamaterial can achieve optimal resonant absorption. Functionalizing the surface with biomolecular receptors further enhances its selectivity for biosensing applications, enabling the detection of biomolecular spectral fingerprints and facilitating real-time, label-free

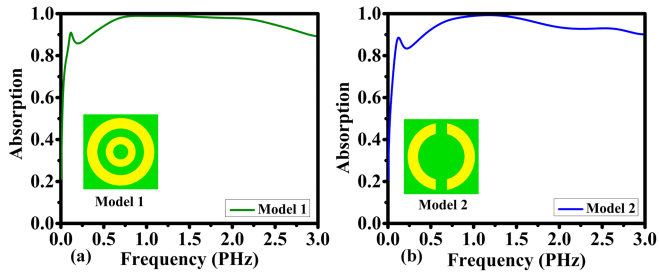

Fig. 2. Comparison of absorption properties between two distinct designs: (a) Absorption properties of model 1, and (b) absorption properties of model 2.

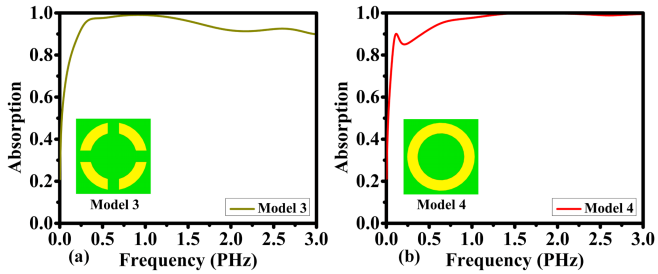

Fig. 3. Comparative analysis of absorption characteristics between two designs: (a) Absorption characteristics of model 3, and (b) absorption characteristics of model 4.

analysis. These high-absorption metamaterials, particularly at specific THz to PHz frequencies, hold significant potential for medical diagnostics. They enable the detection of vibrational signatures with ultra-sensitive resolution, driving advancements in real-time biosensing applications.

III. Absorption Properties and Characteristics

Model 1 and Model 2, shown in Fig. 2, represent two distinct design structures aimed at achieving high absorptivity across the frequency range of 70 THz to 3 PHz. Model 1 features a layout of two concentric circles, designed to maintain high absorptivity across a broad frequency spectrum. From 70 THz to 0.8 PHz, the absorptivity remains consistently above 85%, ensuring effective absorption of electromagnetic waves. Beyond 0.8 PHz, the absorptivity peaks at nearly 100% between 0.8 and 1.8 PHz, efficiently covering a significant portion of the higher frequency spectrum. Although slightly reduced beyond 1.8 PHz, the absorptivity remains high at approximately 90%, extending up to 3 PHz, as shown in Fig. 2(a).

Model 2 employs a simpler single-ring structure with two cuts. Despite its straightforward configuration, Model 2 exhibits comparable absorptivity to Model 1 across the same frequency range. From 70 THz to 1 PHz, the absorptivity is consistently above 85%, ensuring effective absorption in this lower frequency band. Between 1 and 1.5 PHz, Model 2 achieves maximum absorptivity of 100%, indicating complete electromagnetic wave absorption within this range. Beyond 1.5 PHz, the absorptivity remains high at approximately 90%, extending up to 3 PHz, as depicted in Fig. 2(b).

The comparison between Model 1 and Model 2 highlights a balance between complexity and performance. Model 1 offers a broader frequency absorption range due to its dual concentric circle design, while Model 2 achieves similar performance with a simpler single-ring structure. Engineers can select the appropriate model based on specific application requirements, such as desired frequency range and absorption efficiency.

Model 3, shown in Fig. 3, features a single-ring structure with four opposing cuts, optimized for effective absorption of electromagnetic waves within specific frequency bands ranging from 70 THz to 3 PHz. Between 0.25 and 0.5 PHz, Model 3 demonstrates absorptivity reliably above 85%, indicating efficient performance in the lower frequency range. As the frequency increases beyond 0.5 PHz, Model 3 achieves its maximum absorptivity of approximately 100% between 0.5 and 1.5 PHz, effectively covering a significant portion of the mid-range frequency spectrum. Beyond 1.5 PHz, the absorptivity decreases slightly to around 90%, extending up to 3 PHz, as shown in Fig. 3(a).

Model 4, shown in Fig. 3, the proposed design, consists of a simpler circular ring structure aimed at achieving high absorptivity across a broader frequency range. It maintains absorptivity above 85% from 70 THz to 1.5 PHz, effectively covering the infrared spectrum. In the frequency range of 1.5 to 3 PHz, Model 4 achieves its maximum absorptivity of 100%, providing complete electromagnetic wave absorption within the ultraviolet range, as depicted in Fig. 3(b).

Comparison of Models 3 and 4 reveals distinct trade-offs between complexity and performance. Model 3, with its single ring and four cuts, provides optimized absorptivity within specific frequency bands, offering versatility for applications requiring targeted absorption. However, its absorptivity drops beyond 1.5 PHz, limiting its performance in higher frequency ranges. In contrast, Model 4 features a simpler design with wideband absorptivity, covering a broader frequency range from infrared to ultraviolet wavelengths. While Model 4's performance is not as finely tuned for specific bands as Model 3's, its absorptivity exceeds 85% across the entire spectrum from 70 THz to 1.5 PHz and reaches 100% from 1.5 to 3 PHz. This wideband absorptivity, combined with its simplicity, makes Model 4 a practical, cost-effective solution for applications requiring precise absorption control across diverse wavelengths. Its broad-spectrum performance reduces the need for complex tuning, making it ideal for infrared and ultraviolet applications.

IV. Metamaterial Structure and Parameter Analysis

This section examines the design specifics of the proposed metamaterial absorber (MMA) and evaluates how different parameters affect its performance. The focus is on understanding the influence of variations in structural components and material properties on the absorption characteristics and electromagnetic responses of the MMA. Key aspects of the MMA structure are analyzed, and its functionality is explored through detailed simulations.

A. Absorption Spectra and Parameter Simulation

Fig. 4(a) compares the absorption responses of two substrate materials, SiO_2 and TiO_2, over a broad frequency range. The SiO_2 substrate demonstrates exceptional performance, with absorption rates exceeding 85% across the spectrum from

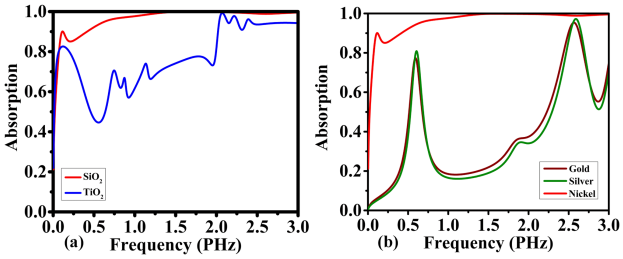

Fig. 4. Absorption spectra of the proposed design under varying substrate and resonator material conditions: (a) Absorption spectra under different substrate materials, and (b) absorption spectra under different resonator materials.

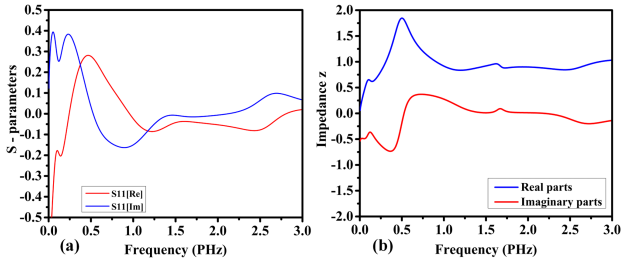

Fig. 5. The simulated responses of parameters of the proposed model: (a) S_{11} real and imaginary parts, and (b) impedance z.

70 THz to 1 PHz. Between 1 PHz and 3 PHz, SiO_2 maintains an impressive 100% absorption efficiency, ensuring effective energy capture across this wide frequency range. This consistent high absorption makes SiO_2 an excellent choice for applications requiring broadband energy absorption. In contrast, TiO_2 exhibits weaker performance in the lower frequency range (70 THz to 2 PHz), where its absorption remains significantly lower than that of SiO_2. However, TiO_2 shows a marked improvement in the 2–3 PHz range, achieving absorption rates above 90%. Despite this high-frequency performance, TiO_2 falls short of the wide-spectrum efficiency demonstrated by SiO_2. These findings emphasize the superiority of SiO_2 as a substrate material for broadband absorption applications.

Fig. 4(b) illustrates the absorption responses of three resonating materials: Nickel, Gold, and Silver. Nickel outperforms the others with absorption exceeding 85% from 70 THz to 1 PHz and reaching 100% absorption from 2 PHz to 3 PHz. In comparison, gold and silver display lower absorption performance, with peaks near 0.5 PHz (less than 80% absorption) and 2.5 PHz (above 90% absorption). However, these peaks are narrow and fail to deliver the broad-spectrum efficiency seen with Nickel.

The differences in absorption performance stem from the inherent material properties. Nickel's structure and composition enable strong resonance and efficient absorption across a wide frequency range, explaining its superior performance. Gold and Silver, while effective at specific frequencies, lack the necessary characteristics for broadband absorption, resulting in their comparatively weaker performance. These results highlight Nickel's potential as a resonating material for applications requiring high absorption efficiency over diverse frequencies, while also showcasing the limitations of Gold and Silver for such purposes.

The analysis investigates the electromagnetic properties of a proposed metamaterial structure designed for ultra-broadband absorption and sensing applications. The reflection coefficient (S_{11}) and complex impedance (z) are analysed to evaluate the structure's absorption efficiency and its suitability for applications like biomedical diagnostics. Fig. 5 illustrates the simulated results, with Fig. 5(a) showing the real and imaginary components of S_{11}, and Fig. 5(b) displaying the real and imaginary parts of the impedance. The S_{11} parameter, which characterizes the reflection behaviour of the structure, is inherently complex. Unlike resonant absorbers that exhibit sharp dips in S_{11} at specific frequencies, this ultra-broadband absorber maintains a consistently low S_{11} magnitude across a wide frequency range, ensuring efficient energy absorption. The real part of S_{11} represents the reflection magnitude, where a consistently low value indicates minimal reflection and high absorption efficiency. The imaginary part of S_{11}, which corresponds to the phase shift of the reflected wave, demonstrates a relatively stable phase response across the bandwidth instead of sharp phase transitions. Negative values in both components of S_{11} arise from the phase of the reflected signal and impedance matching conditions, but these values are distributed across the frequency range and reflect the broadband absorption mechanism rather than being concentrated at specific resonances.

The complex impedance further explains the absorption mechanism. The real part of z represents resistance associated with power dissipation, such as heat, and efficient broadband absorption is achieved when the real part of z is close to unity, indicating optimal impedance matching with the incident medium. This minimizes reflection and maximizes energy coupling into the structure. The imaginary part of z represents reactance, capturing the structure's capacitive and inductive characteristics, and its smooth variation across the frequency range ensures consistent impedance matching over a wide bandwidth. Negative values in the impedance components, which are typical for metamaterials, contribute to broadband impedance matching and do not indicate unphysical behaviour but rather reflect the engineered properties of the material.

The key characteristic of this structure is its ability to maintain high absorption efficiency across a wide frequency range. This is achieved through careful metamaterial design that ensures broadband impedance matching, as evidenced by the smooth, stable responses of both S_{11} and z without sharp resonances or sudden variations. The negative values in both parameters, distributed across the bandwidth, enhance the structure's broadband absorption and sensitivity. This analysis confirms the structure's potential as a high-performance ultra-broadband absorber and sensor, making it highly suitable for applications like biomedical sensing, where signals may span a wide frequency range. Its engineered response ensures efficient operation across diverse wavelength applications, fulfilling the demands of modern nanophotonic and sensing technologies.

B. Permeability, Permittivity, and Simulated Responses

Permeability and permittivity are fundamental properties that significantly influence the performance of absorbers in various fields, including electromagnetic wave absorption, acoustics,

and heat transfer. Permeability determines a material's ability to allow the penetration of specific fields or substances, while permittivity governs its capacity to store electrical energy in response to an applied electric field. These properties are particularly critical in electromagnetic absorbers, such as those used in radar, communication systems, and stealth technology.

In absorbers, optimizing permeability enables efficient absorption across a desired frequency range. Materials with tailored permeability can selectively absorb specific wavelengths while allowing others to pass through, providing precise control over absorption properties. Similarly, tuning permittivity allows for manipulating reflection and absorption characteristics, enhancing the absorber's performance in specific applications. By engineering these properties, absorbers can be customized for diverse purposes, including electromagnetic interference shielding, antenna design, and energy harvesting systems. Thus, understanding and manipulating permeability and permittivity are essential for developing advanced absorbers with tailored profiles and enhanced performance.

The permeability (μ) and permittivity (ε) of the proposed absorber were retrieved following the widely used S-parameter retrieval method, which is based on analyzing the reflection (S_{11}) and transmission (S_{21}) coefficients obtained from simulations or measurements. First, numerical simulations are performed using tools such as CST Studio Suite where the absorber unit cell is modeled with periodic boundary conditions to emulate an infinite array. The S_{11} and S_{12} parameters are computed over the desired frequency range to characterize the electromagnetic response. Next, the effective impedance (Z_{eff}) and refractive index (n_{eff}) are calculated using the simulated S_{11} and S_{12} data. The effective impedance is derived as

$$Z_{eff} = \pm\sqrt{\left[(1+S_{11})^2 - S_{21}^2\right] / \left[(1-S_{11})^2 - S_{21}^2\right]} \quad (1)$$

where the correct sign is chosen to maintain physical consistency. The effective refractive index is determined from the phase of S_{21} using the relationship

$$n_{eff} = arccos\left[\left(1 - S_{11}^2 + S_{21}^2\right) / (2S_{21})\right] / kd \quad (2)$$

where $k = 2\pi/\lambda$ is the wave number, and d is the thickness of the absorber layer.

Once Z_{eff} and n_{eff} are obtained, the effective permeability (μ_{eff}) and permittivity (ε_{eff}) can be calculated using the relationships $\mu_{eff} = n_{eff}Z_{eff}$ and $\varepsilon_{eff} = n_{eff}Z_{eff}$. This process provides a detailed characterization of the absorber's electromagnetic properties, enabling validation and optimization of its design.

Fig. 6(a) depicts the real part of the permeability (μ) and permittivity (ε) of the proposed structure, representing the material's response to applied electric and magnetic fields. The real part values range from -200 to +135, indicating the structure's strong magnetic and electric field responses. Additionally, Fig. 6(a) illustrates the permittivity and permeability (ε and μ) across the terahertz (THz) to petahertz (PHz) frequency range (70 THz to 3 PHz). Within the infrared (IR) spectrum (70–400 THz, or 0.07–0.4 PHz), the sensor exhibits double-negative (DNG) properties, where both permeability and permittivity are negative.

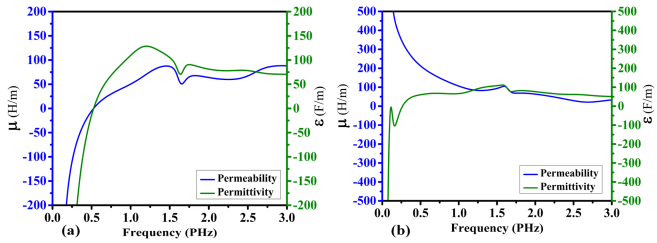

Fig. 6. Real and imaginary parts of permeability (μ) and permittivity (ε) for the proposed absorber: (a) Real parts of μ and ε, and (b) imaginary parts of μ and ε.

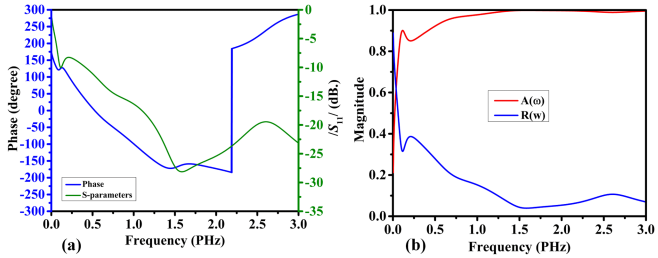

Fig. 7. Simulatd responses of parameters of the proposed model. (a) Phase, and (b) the reflection spectrum and absorption spectrum of the absorber.

The DNG behavior within the IR range enables unique electromagnetic wave manipulation, such as negative refraction and high absorption. This significantly enhances the sensor's ability to absorb incident waves, improving its sensitivity to weak signals. Such sensitivity is critical for detecting low-concentration biomolecules like exosomes—small vesicles containing proteins, lipids, and nucleic acids that serve as important biomarkers for early cancer detection. The IR region is particularly suited for identifying vibrational modes of biomolecules, and the DNG sensor effectively captures exosome signatures due to their unique spectral fingerprints.

Moreover, high absorption and specific resonance within the DNG range minimize interference from non-target frequencies, enhancing selectivity and reducing background noise, which are both essential for accurate diagnostics. Fig. 6(b) shows the imaginary component of the permeability and permittivity response, confirming the structure's proper electromagnetic properties.

The scattering and phase responses up to 3 PHz are shown in Fig. 7(a). The phase response exhibits a shift from positive to negative up to 2.4 PHz, after which it changes behavior. A peak return loss of -27 dB is observed at 1.52 PHz. Fig. 7(b) illustrates the absorption and reflectance responses, which are inversely related. Notably, the absorption exceeds 90% for frequencies above 0.5 PHz.

V. Metamaterial Structure Field Distributions and Surface Current Analysis

This section focuses on understanding the electromagnetic behavior of the designed metamaterial structure. It begins by analyzing the field distributions within the metamaterial, examining both electric and magnetic field components. Subsequently, the section delves into the investigation of surface

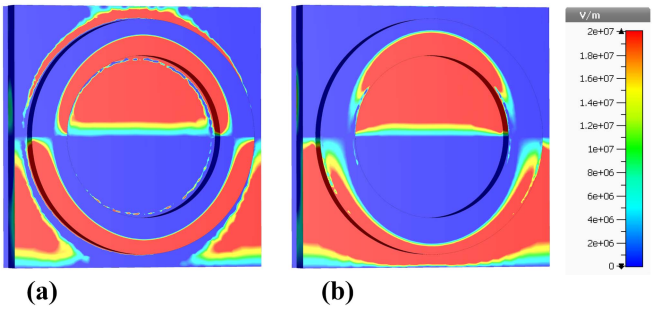

Fig. 8. Visualization of metamaterial structure field distributions on a color map: (a) Real parts of E_z-field, and (b) imaginary parts of E_z-field.

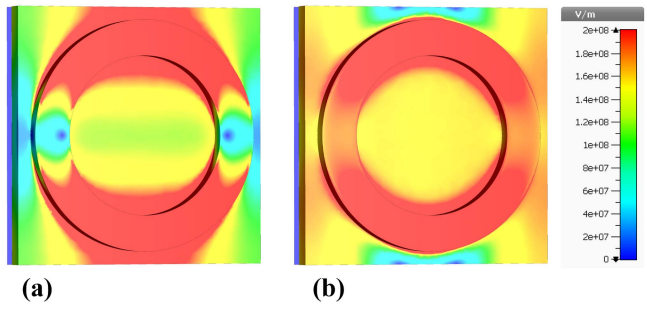

Fig. 9. Visualization of metamaterial structure field distributions on a color map: (a) Real parts of $|E|$-field, and (b) imaginary parts of $|E|$-field.

current distributions, providing insights into the charge flow dynamics within the structure. Finally, the impact of angle modifications, including both incidence and polarization angles, on the absorption characteristics of the metamaterial is explored.

A. *Metamaterial Structure Field Distributions*

Fig. 8 depicts the electric field (E_z) distribution within a broadband, ultra-high-performance metamaterial perfect absorber designed to operate across the terahertz (THz) to petahertz (PHz) spectrum (70 THz to 3 PHz), spanning the mid-infrared (MIR) to extreme ultraviolet (EUV) range. Fig. 8(a) and (b) respectively illustrate the real and imaginary components of the E_z-field, visualized using a color scale where red represents higher values and blue represents lower values. The concentric circular patterns suggest a structured, layered metamaterial design that enhances interaction with incident electromagnetic waves, ensuring efficient absorption across the specified frequency range. Variations in color gradients and disruptions in the patterns correspond to changes in material properties or structural boundaries.

To gain deeper insights into the sensor's performance, CST Studio Suite is used to analyze the E_z-field distribution along the z-axis. The real component of the E_z-field represents the in-phase response, associated with energy storage and directional energy flow (positive for upward, negative for downward). The imaginary component reflects energy loss due to material properties such as resistance or conductivity, with positive values indicating absorption and negative values indicating energy release. By examining both real and imaginary components, it becomes possible to identify regions of high energy storage, visualize energy absorption and loss, and assess the sensor's efficiency and potential heat generation.

Additionally, CST Studio Suites' visualization tools enable the analysis of E_z-field behavior across different planes and frequencies, along with other field components such as the magnetic field (H-field). This comprehensive approach provides valuable insights into the sensor's electromagnetic interactions, functionality, and potential applications.

The absolute value of the electric field ($|E|$-field) distribution is a critical parameter for evaluating the performance of metamaterial perfect absorber sensors. It quantifies the intensity of the electric field at different points within the sensor structure, regardless of direction. By analyzing the $|E|$-field distribution, researchers can identify high-intensity regions that are essential for achieving efficient absorption and high sensitivity.

The $|E|$-field comprises both real and imaginary components. The real part represents the strength and direction of the electric field, while the imaginary part reflects energy dissipation or absorption. These components are influenced by the metamaterial's properties, such as permittivity and permeability.

Fig. 9 visually depicts the $|E|$-field distribution within a nano-metamaterial perfect absorber designed for a broad frequency range. Fig. 9(a) illustrates the real part, highlighting areas of strong electric field amplitude and direction. Fig. 9(b) shows the imaginary part, indicating phase shifts and energy dissipation. These visualizations provide valuable insights into the metamaterial's interaction with electromagnetic waves, identifying regions of energy concentration and loss. This understanding is vital for optimizing the absorber's efficiency and exploring advanced functionalities such as MTM sensors, directional control, wavefront shaping, and cloaking.

To comprehensively understand light absorption in metamaterial perfect absorber sensors, analyzing the magnetic field (H_z-field) on the z-axis using CST Studio Suite is essential. Like the electric field, the H_z-field is a complex quantity with real and imaginary components. The real part represents the in-phase component, indicating magnetic energy storage at various locations within the sensor. Positive values correspond to an upward-pointing magnetic field, contributing to efficient energy storage for light absorption. The imaginary part reflects energy exchange influenced by material properties, with positive values indicating light absorption and negative values signifying energy release back into the field.

Fig. 10 provides a detailed visualization of the H_z-field distributions within the nano-metamaterial structure, designed for broadband and ultra-bandwidth absorption across the 70 THz to 3 PHz range. Fig. 10(a) illustrates the real part of the H_z-field using a color map transitioning from blue at the center to red at the outer edges, representing magnetic field intensities from 0 A/m to 100000 A/m. The central blue area indicates lower field intensity, which gradually increases toward the red periphery. Fig. 10(b) depicts the imaginary part of the H_z-field with a similar color scheme but features a more pronounced central blue region and distinct, thicker concentric rings of green, yellow, and red. This pattern highlights intensity variations and phase

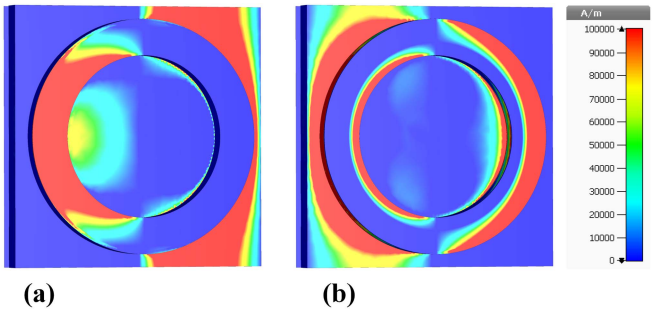

Fig. 10. Visualization of metamaterial structure field distributions on a color map: (a) Real parts of H_z-field, and (b) imaginary parts of H_z-field.

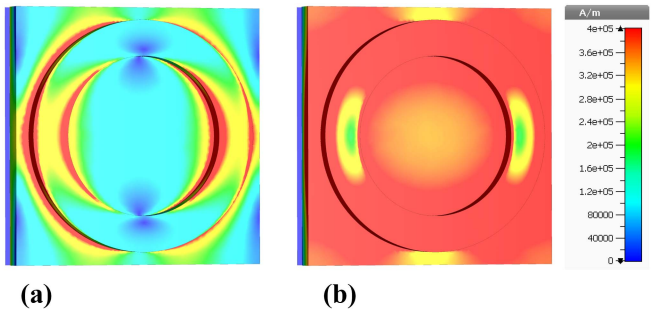

Fig. 11. Visualization of metamaterial structure field distributions on a color map: (a) Real parts of $|H|$-field, and (b) imaginary parts of $|H|$-field.

shifts within the metamaterial, crucial for electromagnetic wave manipulation.

Compared to earlier visualizations of the electric field (E_z-field), these H_z-field analyses provide complementary insights into the magnetic field behavior. Together, they are essential for optimizing the metamaterial's absorption efficiency across the specified spectral range, from infrared to ultraviolet.

Analyzing light absorption in metamaterial perfect absorber sensors involves examining both the electric field (E-field) and the absolute value of the magnetic field ($|H|$-field). While the E-field primarily governs light absorption, the $|H|$-field offers critical insights into magnetic behavior. Using CST Studio, the real component of the $|H|$-field indicates the magnitude and direction of the magnetic field, which is essential for efficient energy storage within the metamaterial. The imaginary component reflects energy exchange due to material properties, with positive values representing energy absorption and negative values indicating energy release. By studying both components across the MIR to EUV spectrum, researchers can optimize metamaterial designs for enhanced electromagnetic wave manipulation and absorption efficiency.

Figs. 11(a) and 11(b) illustrate the magnetic field intensity variations within the nano-metamaterial structure using distinct color maps. Fig. 11(a) shows a swirling pattern with concentric shapes in blue, green, and yellow, representing variations in magnetic field intensity. Fig. 11(b) displays a gradient pattern, transitioning from red at the outer edges to bright yellow and orange toward the center, indicating regions of elevated field intensities. The color scales beside each figure quantify the magnetic field intensity, ranging from 0 A/m to 400000 A/m.

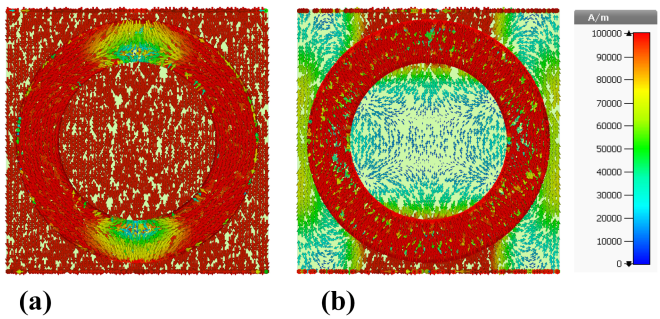

Fig. 12. Surface current distribution of the recommended metamaterial: (a) Real part, and (b) imaginary part.

In Fig. 11(a), the blue and green hues near the center indicate lower magnetic field intensities, while the transition to yellow, orange, and red shades toward the periphery suggests increasing field strength. Similarly, in Fig. 11(b), the red outer edges correspond to areas of high field intensity, gradually shifting to yellow and orange tones at the center. These visualizations provide valuable insights into the spatial distribution and strength of the magnetic field within the metamaterial. Such analyses aid in optimizing the design for specific applications, enhancing absorption efficiency, and improving electromagnetic wave manipulation across the specified frequency range.

B. Surface Current Distribution and Angle Modification Investigation

Fig. 12, depicting the surface current distribution of a nano-metamaterial perfect absorber, complements the earlier Figs. 8 through 11 by providing a detailed visualization of the magnetic field behavior, crucial for understanding the metamaterial's electromagnetic properties.

Fig. 12(a) illustrates the real part of the surface current distribution, with predominant red hues interspersed with blue, green, and yellow, indicating variations in magnetic field intensity. The real part is essential for assessing the in-phase component of the magnetic field, which plays a key role in energy storage within the metamaterial. The blue and green hues in the center represent lower magnetic field intensities, while the red regions toward the periphery indicate higher intensities.

Fig. 12(b) shows the imaginary part of the surface current distribution, characterized by concentric circular patterns transitioning from red at the outer edges to bright yellow and orange toward the center. These transitions highlight regions of higher field intensities, indicating energy absorption and release. The imaginary part reflects energy exchange due to material properties, with positive values representing absorption and negative values indicating release.

The surface current distributions, ranging from 0 A/m to 100000 A/m, align with the earlier Fig. 8 through Fig. 11, which depict magnetic field intensity variations in the nano-metamaterial structure. The color gradients in these figures provide a visual representation of field distribution, aiding in the comprehensive analysis of the metamaterial's electromagnetic behavior. By comparing these visualizations, researchers can

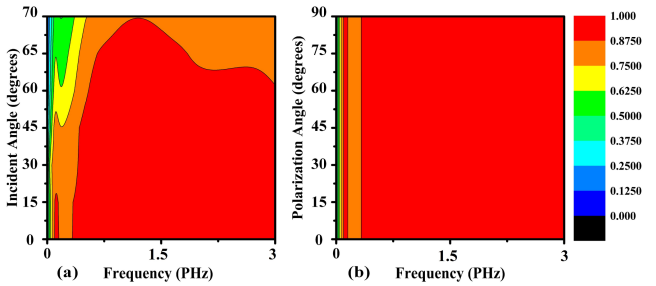

Fig. 13. Investigation of angle modification impact on absorption rate: (a) Incidence angle modification impact, and (b) polarization angle modification impact.

gain deeper insights into spatial patterns, intensity levels, and the overall efficiency of the metamaterial in manipulating and absorbing electromagnetic waves. These analyses facilitate the optimization of sensor performance and functionality across the specified frequency range.

Fig. 13 complements the earlier images by offering an in-depth analysis of the angle-dependent absorption characteristics of the nano-metamaterial perfect absorber. While Fig. 12(a) and (b) focused on the surface current distribution, revealing spatial variations in magnetic field intensity across the structure, Fig. 13 examines the absorber's efficiency concerning changes in incident and polarization angles over the broad frequency range of 70 THz to 3 PHz.

In Fig. 12(a) and (b), vibrant color variations indicated magnetic field intensity levels, with blue and green hues representing lower intensities and red and yellow hues signifying higher intensities. These visualizations highlighted regions within the metamaterial where energy storage and exchange predominantly occurred, offering critical insights into the field distribution necessary for efficient light absorption.

Fig. 13(a) shifts focus to the absorber's performance across varying incidence angles. It demonstrates that the metamaterial maintains high absorption (represented in red) across a wide range of angles, particularly from 0 to 60 degrees. Even at angles beyond 60 degrees, the absorption efficiency remains robust, with only minimal sensitivity, as indicated by the transition to green and yellow hues between 60 and 70 degrees. This performance underscores the absorber's capability to effectively capture electromagnetic waves, even when the incident light deviates significantly from normal incidence.

Fig. 13(b) extends this analysis to polarization angles, revealing consistent high absorption rates across all polarization states. The uniform red coloration throughout indicates that the metamaterial's design ensures robust and polarization-insensitive performance, making it versatile for applications across the MIR to EUV spectrum.

Together, Figs. 12 and 13 highlight the dual strengths of the metamaterial: its detailed internal field distribution, facilitating efficient energy manipulation (Fig. 12(a) and (b)), and its wide-angle performance, ensuring high absorption efficiency under varied incidence and polarization conditions (Fig. 13). This comprehensive analysis underscores the optimized design of the metamaterial for enhanced electromagnetic wave absorption and functionality over a broad frequency range.

VI. Methodology for Sensor Realization

This section focuses on the theoretical design and analysis of a polarization-insensitive nano-metamaterial absorber with a broad spectral response ranging from 70 THz to 3 PHz. Although the design has not yet been fabricated, the proposed methodology lays a robust foundation for real-world implementation. It demonstrates strong potential for practical fabrication using well-established nanotechnology techniques.

The design methodology incorporates advanced theoretical modeling and the CST Studio Suite, a highly accurate industry-standard numerical simulation tool based on finite element method (FEM) analysis. CST Studio Suite was utilized to optimize key performance metrics, including polarization insensitivity, double-negative permittivity (ε) and permeability (μ), angular stability, and high absorption efficiency. Symmetric unit cell geometries, such as split-ring resonators (SRRs) and complementary structures, were iteratively refined to meet stringent performance requirements. This methodology enabled the design to achieve impedance matching and an average absorption rate of 97% across the targeted ultra-wide spectral range.

The material selection and structural design were carefully guided by considerations of real-world fabrication feasibility. Conductive materials such as gold (Au) and silver (Ag) were chosen for their exceptional plasmonic properties and compatibility with well-established deposition techniques. Likewise, dielectric substrates like silicon dioxide (SiO_2) and titanium dioxide (TiO_2) were selected for their low optical loss and mechanical stability, ensuring practical adaptability for fabrication processes.

Although fabrication remains theoretical at this stage, the proposed methodology aligns closely with existing nanofabrication techniques. Thin-film deposition can be precisely achieved using methods such as electron-beam evaporation, sputtering, or atomic layer deposition. Resonator structures can be accurately patterned with electron-beam lithography (EBL) or nanoimprint lithography (NIL), followed by techniques like reactive ion etching (RIE) or focused ion beam (FIB) milling to define nanostructures. These methods are well-documented, scalable, and reinforce the sensor's practicality for large-scale manufacturing.

The sensor's compact design and simplicity further enhance its feasibility for integration into advanced diagnostic systems. Its compatibility with scalable techniques, such as roll-to-roll nanoimprint lithography, positions it as a strong candidate for real-world biomedical applications. Future research could experimentally validate the design and explore advanced materials, such as graphene and 2D semiconductors, to enhance performance and extend its operational range.

This work highlights the strong potential of the proposed sensor for practical fabrication, laying the foundation for its application in innovative biomedical technologies, particularly in non-invasive cancer diagnostics.

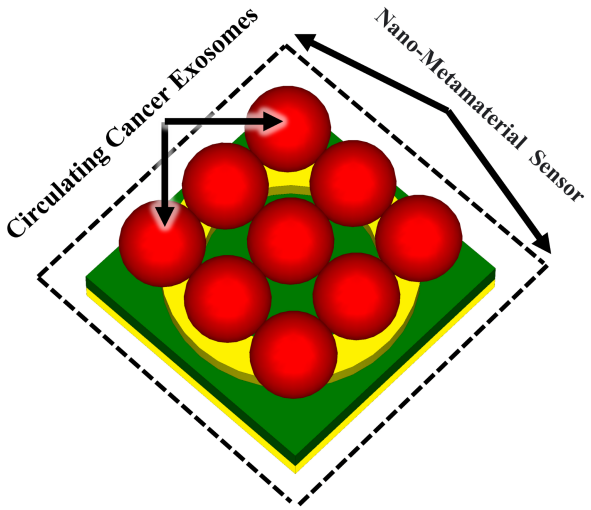

Fig. 14. Nano-Metamaterial biosensor configuration illustrating the distribution and interactions of electric and magnetic fields within both circulating cancerous and normal exosomes.

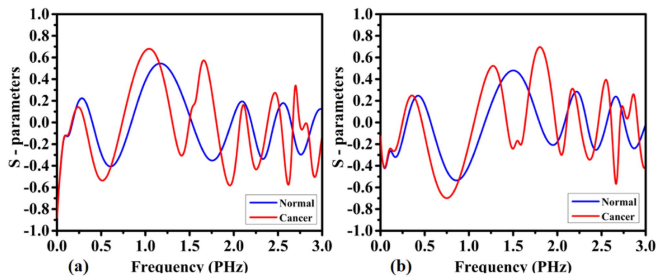

Fig. 15. Nano-Metamaterial biosensor evaluation for distinguishing normal versus cancerous exosomes over the spectral range from 70 THz to 3 PHz: (a) Real component of S_{11}, and (b) imaginary component of S_{11}.

VII. Detection of Circulating Cancer Exosomes

Fig. 14 illustrates the configuration of the nano-metamaterial biosensor designed for detecting circulating cancer exosomes. In the figure, red spheres represent cancer exosomes positioned on the sensor, emphasizing the interaction between the exosomes and the sensor's electric and magnetic fields. The sensor's nano-metamaterial layer is engineered to exhibit unique electromagnetic properties, specifically negative permittivity and permeability (double-negative properties) in the near-infrared (NIR) range, spanning 70 THz to 400 THz. These double-negative properties enable the sensor to interact strongly with electromagnetic fields in the target frequency range, enhancing its sensitivity to subtle variations in exosome characteristics. Additionally, the sensor's structure ensures polarization insensitivity, allowing it to operate effectively regardless of the incoming light's polarization.

Fig. 15 presents the analysis of the S-parameter (S_{11}) for the nano-metamaterial biosensor, demonstrating its ability to distinguish between normal and cancerous exosomes across the spectral range of 70 THz to 3 PHz. The S_{11} parameter, representing the reflection coefficient, indicates the amount of electromagnetic wave reflected by the sensor.

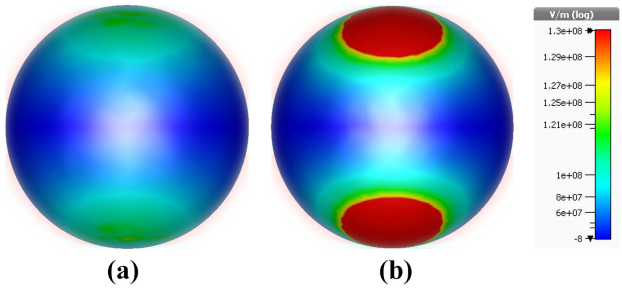

Fig. 16. Microwave imaging (MWI) of the electric field (E-field) at 100 THz as detected by the near-infrared biosensor, showcasing exosome analysis: (a) Normal exosomes, and (b) cancerous exosomes.

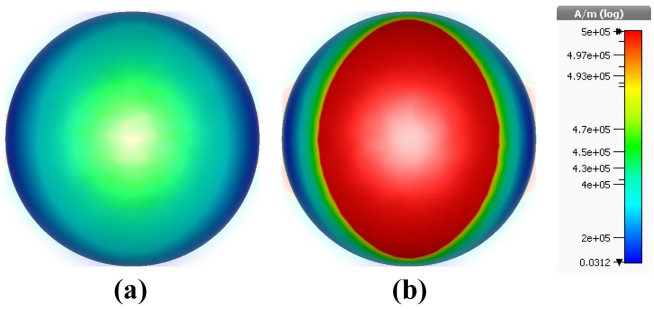

Fig. 17. MWI visualization of the magnetic field (H-field) at 400 THz, examining exosomes with the near-infrared biosensor: (a) Normal exosomes, and (b) cancerous exosomes.

Fig. 15(a) displays the real component of S_{11}, with the red line representing cancerous exosomes and the blue line representing normal exosomes. Noticeable differences in the peaks and troughs between the two lines reveal variations in how the sensor interacts with cancerous versus normal exosomes. This distinction highlights the sensor's capability to differentiate between the two types based on the unique electromagnetic properties of cancerous exosomes.

Fig. 15(b) shows the imaginary component of S_{11} over the same frequency range, illustrating distinct profiles for cancerous and normal exosomes. These differences are significant because the imaginary component of S_{11} is related to energy absorption and loss, which vary between different exosome types.

By analyzing both the real and imaginary components of S_{11}, the sensor captures a comprehensive electromagnetic signature of the exosomes. This dual-component analysis enhances the sensor's sensitivity and precision in distinguishing cancerous exosomes from normal ones, making it a powerful tool for early cancer detection.

Microwave imaging (MWI) offers a non-invasive approach for detecting and differentiating cancerous exosomes by analyzing their interactions with electromagnetic fields. Figs. 16 and 17 illustrate the MWI analysis of the electric field (*E*-field) at 100 THz and the magnetic field (*H*-field) at 400 THz, respectively, for normal and cancerous exosomes. These images reveal significant contrasts in field intensities, enabling clear differentiation between the two.

In Fig. 16(a), the *E*-field distribution for normal exosomes is relatively uniform and low in intensity (blue/green on a

TABLE II
COMPARATIVE ANALYSIS WITH RELEVANT WORK

Ref.	Material	Unit cell Dimension (nm)	Operation Range (PHz)	Bandwidth (PHz)	Angular Stability	Absorption
[54]	Ni, SiO_2	200×200×96	0.1- 1.39	1.29	80% absorption for $\theta \leq 60$	95.91%
[55]	Ni, SiO_2	300×300×170	0.18- 0.99	0.81	70% absorption for $\theta \leq 70$	>91.27 %
[56]	Ni, SiO_2	200×200×125	0.11 - 0.75	0.64	80% absorption for $\theta \leq 60$	93 %
[57]	W, SiO_2	200×200×242	0.12 - 0.75	0.63	80% absorption for $\theta \leq 45$	92 %
[58]	W, Al_2O_3, Ti	1000×1000×320	0.16 - 0.6	0.44	94% absorption for $\theta \leq 60$	94 %
[59]	Ni, AlN	75×75×50	0.1 - 0.75	0.65	70% absorption for $\theta \leq 60$	90 %
[60]	Ti, SiO_2, Si_3N_4	750×750×550	0.10 - 0.36	0.26	85% absorption for $\theta \leq 60$	95 %
[61]	Cr, SiO_2	160×160×85	0.39 - 0.75	0.36	80% absorption for $\theta \leq 60$	96 %
Proposed	Ni, SiO_2	100×100×23	0.07 - 3	2.93	80% absorption for $\theta \leq 70$	>97 %

logarithmic scale), indicating weak electromagnetic interactions at 100 THz. In contrast, Fig. 16(b) shows cancerous exosomes with significantly higher *E*-field intensities (red areas), concentrated at the poles, reflecting their distinct electromagnetic properties. These heightened interactions arise from differences in dielectric properties, membrane proteins, and other molecular components unique to cancerous cells.

Similarly, Fig. 17(a) depicts a low-intensity and uniform *H*-field distribution for normal exosomes at 400 THz, indicating minimal magnetic interactions. However, Fig. 17(b) reveals markedly higher *H*-field intensities for cancerous exosomes, particularly concentrated at the center. This enhanced magnetic response results from unique molecular markers in cancerous exosomes, such as altered protein content and conductivity.

The differences in *E*-field and *H*-field intensities are key biophysical parameters for identifying cancerous exosomes. Normal exosomes exhibit minimal field interactions, serving as a baseline, while cancerous exosomes display heightened electromagnetic responses.

MWI's ability to visualize these distinctions makes it a promising tool for early cancer diagnosis. The field intensity variations provide critical diagnostic insights into the structural and molecular disparities between normal and cancerous exosomes, paving the way for more precise and non-invasive diagnostic methodologies.

VIII. ADVANTAGES OF THE PROPOSED DESIGN

The proposed polarization-insensitive nano-metamaterial sensor offers several advantages over previously reported designs, particularly in its application for detecting circulating cancer exosomes (CCEs). Operating across an ultra-wide frequency range of 70 THz to 3 PHz, the sensor achieves an impressive average absorption efficiency exceeding 97%, as demonstrated in Table II. This exceptional performance ensures high sensitivity and accuracy in distinguishing the electromagnetic responses of cancerous and normal exosomes, making it a highly effective tool for early-stage cancer diagnostics.

In addition to its outstanding sensitivity, the sensor's compact and fabrication-friendly design, combined with its non-invasive, label-free detection method, enhances its practicality for real-world applications. Unlike many existing solutions, it exhibits remarkable angular stability, maintaining reliable performance under incident angles of up to 70°, as highlighted in Table III. These distinguishing features, supported by detailed performance comparisons provided in Tables II through V, underscore the sensor's potential as a significant advancement in metamaterial-based diagnostic technologies.

IX. BENCHMARKING

Designing a broadband metamaterial absorber (MTMA) that operates across the mid-infrared (MIR) to ultraviolet (UV) spectrum while ensuring compactness, polarization insensitivity, high absorption rates, and angular stability is inherently challenging. However, the proposed design demonstrates superior performance compared to recently reported absorbers (Table II). With an ultra-wide operating range of 70 THz to 3 PHz, the sensor achieves an impressive average absorption rate exceeding 97% across the entire range (Table II). Its unique design leverages double-negative metamaterial properties (negative permittivity and permeability) in the near-infrared (NIR) range (70 THz to 400 THz), enhancing sensitivity for early-stage cancer detection through exosome analysis.

The sensor's applications extend across multiple spectral regions, each supporting critical functionalities in biomedical engineering, energy harvesting, and molecular diagnostics:

- NIR (70 THz–400 THz): Optimized for non-invasive imaging techniques like optical coherence tomography (OCT) and NIR spectroscopy, essential for early cancer detection.
- Visible Spectrum: Facilitates high-resolution imaging for identifying cancer biomarkers.
- UV (near- to mid-UV range): Enables detailed DNA and protein analysis for profiling cancer-specific biomarkers in exosomes.
- Far-UV: Provides molecular fingerprinting for detecting biomolecular changes associated with cancer.

The sensor's consistent absorption performance at incident angles between 0° and 70° ensures reliable functionality in various practical applications, making it highly versatile for diagnostic and environmental monitoring tasks.

These features position the nano-metamaterial absorber as a leading candidate for applications ranging from personalized healthcare to pollutant detection. Its superior bandwidth, sensitivity, and angular stability not only surpass existing MTMA

TABLE III
DISTINCTIVE FEATURES OF THE PROPOSED NANO-METAMATERIAL SENSOR DESIGN

Aspect	Proposed Sensor	Unique Achievement
Design Complexity	Simple and minimalistic	Achieved high-performance results with a straightforward design, avoiding the challenges of complex structures.
Fabrication Feasibility	Highly feasible at the nanoscale	Simplified design enables efficient and cost-effective fabrication at the nanoscale, overcoming common difficulties.
Size	Ultra-compact	Significantly smaller than most competing designs, facilitating integration into portable diagnostic systems.
Performance Efficiency	>97% absorption rate	Delivered exceptional absorption efficiency across the ultra-wideband range, despite a compact design.
Nanoscale Manufacturing	Easily scalable	Fabrication-friendly structure ensures repeatability and scalability for large-scale production.
Double-Negative Characteristics	Achieved in the NIR range (70–400 THz)	Combines negative permittivity and permeability without requiring intricate geometries.
Angular Stability	Consistent up to 70°	Maintains excellent performance under varying angles, a rare feature for compact designs.
Biomedical Applications	Non-invasive cancer diagnostics	Delivers high sensitivity for exosome detection, combining nanoscale precision with outstanding results.
Design Innovation	Simplicity with high functionality	Demonstrates that simplicity in design does not compromise advanced functionality, setting a new benchmark.

TABLE IV
UNIQUE FEATURES OF THE PROPOSED NANO-METAMATERIAL SENSOR

Feature	Proposed Sensor	Novelty Aspect
Ultra-Wide Operating Range	70 THz – 3 PHz	Achieves a significantly broader bandwidth compared to existing sensors in the same domain.
Average Absorption Rate (%)	97%	Exceptional absorption efficiency across the entire range, surpassing benchmarks.
Polarization Insensitivity	Yes	Maintains performance regardless of the polarization angle, ensuring versatility in applications.
Angular Stability	Consistent (0°–70°)	High angular stability ensures reliable performance for practical diagnostic scenarios.
Double-Negative Properties	Negative ε and μ (70–400 THz)	Integration of double-negative metamaterials enhances sensitivity specifically for NIR detection.
Biomedical Target	Cancer exosomes detection	Focuses on non-invasive, label-free detection of circulating cancer exosomes (CCEs).
Application Versatility	NIR, Visible, UV, and MIR ranges	Supports diverse functionalities, including imaging, DNA/protein analysis, and molecular diagnostics.
Compact Design	Highly compact nano-metamaterial	Enables integration into portable diagnostic systems for personalized healthcare.
Non-Invasive Detection	Yes	Facilitates early cancer detection without requiring invasive procedures.
Label-Free Detection	Yes	Eliminates the need for additional labeling agents, simplifying biomarker identification.

TABLE V
DOUBLE-NEGATIVE CHARACTERISTICS OF THE PROPOSED SENSOR IN THE 70 THZ TO 400 THZ RANGE

Characteristic	Proposed Sensor	Novel Aspect
Frequency Range	70 THz – 400 THz	Covers the critical near-infrared (NIR) spectrum for biomedical applications.
Permittivity (ε)	Negative	Demonstrates negative permittivity, enabling unique wave manipulation capabilities.
Permeability (μ)	Negative	Achieves negative permeability, enhancing resonance behavior and sensor sensitivity.
Double-Negative Property (DNG)	Yes (Negative ε and μ)	Combines both negative permittivity and permeability in the NIR range, a feature absent in most designs.
Absorption Rate in NIR Range	>97%	Exceptional absorption efficiency due to the double-negative properties.
Biomedical Relevance	Optimized for cancer exosome detection	High sensitivity to detect circulating cancer exosomes (CCEs) through resonance frequency shifts.
Application Versatility	Non-invasive cancer diagnostics	Facilitates early-stage cancer detection with minimal interference, leveraging NIR capabilities.
Design Innovation	Compact and polarization-insensitive	Unites compactness, angular stability, and double-negative characteristics in the NIR spectrum.

designs but also align with recent advancements in 2024 studies, setting a benchmark for future innovations in broadband metamaterial technology.

Key Advancements Highlighted in Tables III, IV, and V:

- Ultra-wide Operating Range (Table III): The sensor spans 70 THz to 3 PHz, covering NIR, MIR, and UV spectra, making it suitable for diverse applications like imaging and molecular diagnostics.
- High Absorption Efficiency (Table III): Achieves an exceptional absorption rate of 97%.
- Double-Negative Properties (Table IV): Negative permittivity (ε) and permeability (μ) in the NIR range enable enhanced wave manipulation and resonance behavior, crucial for detecting circulating cancer exosomes (CCEs) with high sensitivity.
- Polarization Insensitivity and Angular Stability (Tables III & V): Maintains high performance up to a 70° incident angle, ensuring reliability in practical scenarios.
- Non-Invasive and Label-Free Detection (Table III): Simplifies workflows by eliminating the need for biopsies or labeling agents, enhancing patient comfort.
- Scalability and Cost-Effectiveness (Table V): Features a compact design suitable for cost-efficient production and integration into portable diagnostic systems.

By uniting high performance, versatility, and practicality, the proposed nano-metamaterial sensor establishes a new standard for biomedical applications, particularly in early cancer detection.

X. FUTURE PERSPECTIVE

Future research will focus on exploring innovative materials to enhance sensor performance, integrating metamaterial absorbers (MTMAs) with nanophononics to develop compact devices, and achieving dynamic tunability for adaptive applications. Key areas of interest include expanding functionalities

for polarization control, nonlinear optics, and biosensing, while addressing the challenges of large-scale manufacturing to enable practical industry deployment.

A significant research direction will involve further exploring the sensor's potential in non-invasive cancer diagnostics, particularly through exosome analysis. Investigating its integration with other diagnostic modalities, such as optical coherence tomography (OCT) and near-infrared spectroscopy, could lead to the development of more robust and precise systems for early cancer detection. Scaling up the sensor design to support real-time, high-throughput diagnostics could significantly enhance its clinical applications.

Efforts to improve the sensor's tunability across broader frequency ranges, including the visible and far-ultraviolet regions, could unlock new possibilities in molecular profiling and environmental monitoring. Additionally, exploring the sensor's adaptability for personalized healthcare and pollutant detection could drive its deployment in both medical and environmental sectors. These advancements would establish the sensor as a versatile tool for biomolecular analysis and real-time monitoring, offering transformative applications across diverse fields.

XI. Conclusion

In this study, we present a polarization-insensitive nano-metamaterial sensor designed for early cancer detection through exosome analysis, operating across a broad spectral range from 70 THz to 3 PHz. The sensor uniquely combines double-negative properties (negative permittivity and permeability) in the near-infrared region, enabling enhanced sensitivity and specificity for identifying circulating cancer exosomes (CCEs). By incorporating microwave imaging (MWI) techniques, we developed a non-invasive, label-free detection method capable of distinguishing cancerous exosomes from normal ones based on their distinct electromagnetic field responses.

To ensure the reliability of our findings, we employed state-of-the-art computational techniques, including finite element method (FEM) and finite-difference time-domain (FDTD) simulations. These well-established methods are widely used for analyzing high-frequency electromagnetic phenomena. Our simulations were meticulously conducted using fine meshes and advanced material models, ensuring high accuracy and reproducibility of results.

Our results demonstrate that the sensor achieves an average absorption rate of 97%, highlighting its ability to detect subtle differences in both the electric (E-field) and magnetic (H-field) interactions of exosomes at high frequencies. Analysis of the real and imaginary components of the S_{11} parameter further underscores the sensor's capability to distinguish between normal and cancerous exosomes by capturing their unique electromagnetic signatures. Validation through E-field analysis at 100 THz and H-field analysis at 400 THz revealed significantly stronger field responses for cancerous exosomes compared to normal ones.

This nano-metamaterial sensor represents a significant advancement in cancer diagnostics, providing a practical, non-invasive approach for early cancer detection. Its high sensitivity to the specific electromagnetic properties of cancerous exosomes holds the potential to enable timely diagnoses, facilitate personalized healthcare strategies, and improve patient outcomes. Future research could explore the sensor's applicability across different cancer types, further enhance its sensitivity, and investigate its integration with clinical imaging systems, establishing it as a versatile tool for early-stage cancer diagnostics.

Competing Interests

The authors declare no competing interests.

Data Availability

The datasets used and/or analyzed during the current study are available from the corresponding author on reasonable request.

References

[1] F. Bendelala, A. Cheknane, and H. S. Hilal, "A broad-band polarization-insensitive absorber with a wide angle range metamaterial for thermo-photovoltaic conversion," *Opt. Quantum Electron.*, vol. 50, pp. 1–10, 2018.
[2] V. Veselago, L. Braginsky, V. Shklover, and C. Hafner, "Negative refractive index materials," *J. Comput. Theor. Nanoscience*, vol. 3, no. 2, pp. 189–218, 2006.
[3] S. P. Rodrigues, S. Lan, L. Kang, Y. Cui, and W. Cai, "Nonlinear imaging and spectroscopy of chiral metamaterials," *Adv. Mater.*, vol. 26, no. 35, pp. 6157–6162, 2014.
[4] J. B. Pendry, "Negative refraction makes a perfect lens," *Phys. Rev. Lett.*, vol. 85, no. 18, 2000, Art. no. 3966.
[5] W. Cai, U. K. Chettiar, A. V. Kildishev, and V. M. Shalaev, "Optical cloaking with metamaterials," *Nature Photon.*, vol. 1, no. 4, pp. 224–227, 2007.
[6] M. M. Hasan, M. R. I. Faruque, and M. T. Islam, "Dual band metamaterial antenna for LTE/bluetooth/WiMAX system," *Sci. Rep.*, vol. 8, no. 1, 2018, Art. no. 1240.
[7] J. Alam, M. R. I. Faruque, and M. T. Islam, "Labyrinth double split open loop resonator based bandpass filter design for S, C and X-band application," *J. Phys. D: Appl. Phys.*, vol. 51, no. 26, 2018, Art. no. 265102.
[8] L. Huang, S. Zhang, and T. Zentgraf, "Metasurface holography: From fundamentals to applications," *Nanophotonics*, vol. 7, no. 6, pp. 1169–1190, 2018.
[9] N. Landy, C. Bingham, T. Tyler, N. Jokerst, D. Smith, and W. Padilla, "Design, theory, and measurement of a polarization-insensitive absorber for terahertz imaging," *Phys. Rev. B*, vol. 79, no. 12, 2009, Art. no. 125104.
[10] S. Hossain et al., "Double-E-triple-H-shaped NRI-metamaterial for dual-band microwave sensing applications," *Comput., Mater. Continua*, vol. 71, no. 3, pp. 5817–5836, 2022.
[11] S. Mahmud, S. S. Islam, A. F. Almutairi, and M. T. Islam, "A wide incident angle, ultrathin, polarization-insensitive metamaterial absorber for optical wavelength applications," *IEEE Access*, vol. 8, pp. 129525–129541, 2020.
[12] M. Y. Azab, M. F. O. Hameed, A. M. Nasr, and S. Obayya, "Highly sensitive metamaterial biosensor for cancer early detection," *IEEE Sensors J.*, vol. 21, no. 6, pp. 7748–7755, Mar. 2021.
[13] S. K. Patel, J. Surve, and J. Parmar, "Detection of cancer with graphene metasurface-based highly efficient sensors," *Diamond Related Mater.*, vol. 129, 2022, Art. no. 109367.
[14] M. N. Hamza et al., "Designing a high-sensitivity microscale triple-band biosensor based on terahertz MTMs to provide a perfect absorber for non-melanoma skin cancer diagnostic," *IEEE Photon. J.*, vol. 16, no. 2, Apr. 2024, Art. no. 5900113.
[15] B. Amini and Z. Atlasbaf, "Design and analysis of high-sensitivity tunable graphene sensors for cancer detection," *Opt. Quantum Electron.*, vol. 55, no. 5, 2023, Art. no. 446.
[16] P. Upender and A. Kumar, "THz dielectric metamaterial sensor with high Q for biosensing applications," *IEEE Sensors J.*, vol. 23, no. 6, pp. 5737–5744, Mar. 2023.
[17] M. N. Hamza and M. T. Islam, "Design of MTM-based multi-band micro-biosensor in terahertz region as perfect absorber for early-stage leukemia diagnosis with sensitivity 18626373 THz/RIU," *IEEE Sensors J.*, vol. 24, no. 10, pp. 16055–16069, May 2024.

[18] Z. Geng, X. Zhang, Z. Fan, X. Lv, and H. Chen, "A route to terahertz metamaterial biosensor integrated with microfluidics for liver cancer biomarker testing in early stage," *Sci. Rep.*, vol. 7, no. 1, 2017, Art. no. 16378.

[19] S. Banerjee, U. Nath, P. Dutta, A. V. Jha, B. Appasani, and N. Bizon, "A theoretical terahertz metamaterial absorber structure with a high quality factor using two circular ring resonators for biomedical sensing," *Inventions*, vol. 6, no. 4, 2021, Art. no. 78.

[20] H. E. Nejad, A. Mir, and A. Farmani, "Supersensitive and tunable nano-biosensor for cancer detection," *IEEE Sensors J.*, vol. 19, no. 13, pp. 4874–4881, Jul. 2019.

[21] D. Li et al., "Identification of early-stage cervical cancer tissue using metamaterial terahertz biosensor with two resonant absorption frequencies," *IEEE J. Sel. Topics Quantum Electron.*, vol. 27, no. 4, Jul./Aug. 2021, Art. no. 8600107.

[22] S. Banerjee, P. Dutta, A. V. Jha, B. Appasani, and M. S. Khan, "A biomedical sensor for detection of cancer cells based on terahertz metamaterial absorber," *IEEE Sensors Lett.*, vol. 6, no. 6, Jun. 2022, Art. no. 6002004.

[23] M. N. Hamza and M. T. Islam, "Designing an extremely tiny dual-band biosensor based on MTMs in the terahertz region as a perfect absorber for non-melanoma skin cancer diagnostics," *IEEE Access*, vol. 11, pp. 136770–136781, 2023.

[24] A. Chaudhuri, B. Rai, and P. Pal, "Design of a dual-band metasurface cross-polarization converter for cancer detection in the terahertz band," *IEEE Sensors J.*, vol. 24, no. 6, pp. 7292–7298, Jun. 2023.

[25] M. N. Hamza, M. T. Islam, and S. Koziel, "Advanced sensor for non-invasive breast cancer and brain cancer diagnosis using antenna array with metamaterial-based AMC," *Eng. Sci. Technol., an Int. J.*, vol. 56, 2024, Art. no. 101779.

[26] J. Chen, F. Hu, X. Ma, M. Yang, S. Lin, and A. Su, "Deep neural network assisted terahertz metasurface sensors for the detection of lung cancer biomarkers," *IEEE Sensors J.*, vol. 24, no. 10, pp. 15698–15705, May 2024.

[27] M. N. Hamza, M. T. Islam, S. Lavadiya, S. Koziel, I. Ud Din, and B. Sanches, "Designing a high-sensitivity dual-band nano-biosensor based on petahertz MTMs to provide a perfect absorber for early-stage non-melanoma skin cancer diagnostic," *IEEE Sensors J.*, vol. 24, no. 11, pp. 18418–18427, Jun. 2024.

[28] A. Hlali, A. Oueslati, and H. Zairi, "Numerical simulation of tunable terahertz graphene-based sensor for breast tumor detection," *IEEE Sensors J.*, vol. 21, no. 8, pp. 9844–9851, Apr. 2021.

[29] M. N. Hamza, S. Koziel, and A. Pietrenko-Dabrowska, "Design and experimental validation of a metamaterial-based sensor for microwave imaging in breast, lung, and brain cancer detection," *Sci. Rep.*, vol. 14, no. 1, 2024, Art. no. 16177.

[30] X. Hou et al., "Cancer biomarkers ultrasensitive detection based on terahertz frequency-comb-like," *IEEE Sensors J.*, vol. 23, no. 10, pp. 10413–10419, May 2023.

[31] M. N. Hamza et al., "Development of a terahertz metamaterial microbiosensor for ultrasensitive multispectral detection of early-stage cervical cancer," *IEEE Sensors J.*, vol. 24, no. 20, pp. 32065–32079, Oct. 2024.

[32] A. Veeraselvam, G. N. A. Mohammed, K. Savarimuthu, and P. D. Vijayaraman, "An ultra-thin multiband refractive index-based carcinoma sensor using THz radiation," *IEEE Sensors J.*, vol. 22, no. 3, pp. 2045–2052, Feb. 2022.

[33] M. N. Hamza et al., "Ultra-compact quintuple-band terahertz metamaterial biosensor for enhanced blood cancer diagnostics," *PLoS One*, vol. 20, no. 1, 2025, Art. no. e0313874.

[34] D. Xie et al., "Terahertz metamaterial biosensor with double resonant frequencies for specific detection of early-stage hepatocellular carcinoma," *IEEE Sensors J.*, vol. 23, no. 2, pp. 1124–1131, Jan. 2023.

[35] F. Wahaia et al., "Detection of colon cancer by terahertz techniques," *J. Mol. Struct.*, vol. 1006, no. 1-3, pp. 77–82, 2011.

[36] M. N. Hamza et al., "Terahertz dual-band metamaterial biosensor for cervical-cancer diagnostics," *IEEE Photon. J.*, vol. 16, no. 5, Oct. 2024, Art. no. 6803011.

[37] C. Tan et al., "Cancer diagnosis using terahertz-graphene-metasurface-based biosensor with dual-resonance response," *Nanomaterials*, vol. 12, no. 21, 2022, Art. no. 3889.

[38] Z. Huang et al., "High-resolution metalens imaging polarimetry," *Nano Lett.*, vol. 23, no. 23, pp. 10991–10997, 2023.

[39] M. Deng et al., "Dielectric metasurfaces for broadband phase-contrast relief-like imaging," *Nano Lett.*, vol. 24, no. 46, pp. 14641–14647, 2024.

[40] D. Wang et al., "Temperature tunable broadband filter based on hybridized vanadium dioxide (VO_2) metasurface," *J. Phys. D: Appl. Phys.*, vol. 58, no. 3, 2024, Art. no. 035106.

[41] N. I. Landy, S. Sajuyigbe, J. J. Mock, D. R. Smith, and W. J. Padilla, "Perfect metamaterial absorber," *Phys. Rev. Lett.*, vol. 100, no. 20, 2008, Art. no. 207402.

[42] S. Mahmud, S. S. Islam, K. Mat, M. E. Chowdhury, H. Rmili, and M. T. Islam, "Design and parametric analysis of a wide-angle polarization-insensitive metamaterial absorber with a star shape resonator for optical wavelength applications," *Results Phys.*, vol. 18, 2020, Art. no. 103259.

[43] D. Lee et al., "Polarization-sensitive tunable absorber in visible and near-infrared regimes," *Sci. Rep.*, vol. 8, no. 1, 2018, Art. no. 12393.

[44] S. Mahmud et al., "A multi-band near perfect polarization and angular insensitive metamaterial absorber with a simple octagonal resonator for visible wavelength," *IEEE Access*, vol. 9, pp. 117746–117760, 2021.

[45] M. M. K. Shuvo, M. I. Hossain, S. Rahman, S. Mahmud, S. S. Islam, and M. T. Islam, "A wide-angle, enhanced oblique incidence, bend-able metamaterial absorber employed in visible region with a sun shape resonator," *IEEE Access*, vol. 9, pp. 126466–126480, 2021.

[46] H. Wang et al., "Broadband tunability of polarization-insensitive absorber based on frequency selective surface," *Sci. Rep.*, vol. 6, no. 1, 2016, Art. no. 23081.

[47] X. Yin et al., "Symmetry-broken square silicon patches for ultra-narrowband light absorption," *Sci. Rep.*, vol. 9, no. 1, 2019, Art. no. 17477.

[48] L. Wu, L. Yang, X. Zhu, B. Cai, and Y. Cheng, "Ultra-broadband and wide-angle plasmonic absorber based on all-dielectric gallium arsenide pyramid nanostructure for full solar radiation spectrum range," *Int. J. Thermal Sci.*, vol. 201, 2024, Art. no. 109043.

[49] S. Feng et al., "Tri-band terahertz metamaterial absorber based on structural $Ti_3C_2T_x$ MXene for enhanced sensing application," *IEEE Sensors J.*, vol. 24, no. 18, pp. 28889–28896, Sep. 2024.

[50] W. Yang et al., "Efficiency tunable terahertz graphene metasurfaces for reflective single/dual-focusing effects based on Pancharatnam-Berry phase," *Results Phys.*, vol. 65, 2024, Art. no. 108003.

[51] J. Li et al., "Full-color enhanced second harmonic generation using rainbow trapping in ultrathin hyperbolic metamaterials," *Nature Commun.*, vol. 12, no. 1, 2021, Art. no. 6425.

[52] R. Contractor, G. D'Aguanno, and C. Menyuk, "Ultra-broadband, polarization-independent, wide-angle absorption in impedance-matched metamaterials with anti-reflective moth-eye surfaces," *Opt. Exp.*, vol. 26, no. 18, pp. 24031–24043, 2018.

[53] S. K. Patel, S. Charola, J. Parmar, and M. Ladumor, "Broadband metasurface solar absorber in the visible and near-infrared region," *Mater. Res. Exp.*, vol. 6, no. 8, 2019, Art. no. 086213.

[54] I. H. Chowdhury, M. M. R. Mazumder, S. S. Islam, M. T. Islam, M. S. Soliman, and M. S. Islam, "Ultrawideband nanostructured metamaterial absorber with an octagon-packed star-shaped resonator for UV to NIR spectrum wavelength application," *Ain Shams Eng. J.*, vol. 31, 2024, Art. no. 102653.

[55] M. M. K. Shuvo et al., "Polarization and angular insensitive bendable metamaterial absorber for UV to NIR range," *Sci. Rep.*, vol. 12, no. 1, 2022, Art. no. 4857.

[56] R. M. H. Bilal, M. A. Saeed, M. A. Naveed, M. Zubair, M. Q. Mehmood, and Y. Massoud, "Nickel-based high-bandwidth nanostructured metamaterial absorber for visible and infrared spectrum," *Nanomaterials*, vol. 12, no. 19, 2022, Art. no. 3356.

[57] A. Musa et al., "Broadband plasmonic metamaterial optical absorber for the visible to near-infrared region," *Nanomaterials*, vol. 13, no. 4, 2023, Art. no. 626.

[58] S. Jiao, Y. Li, H. Yang, and S. Xu, "Numerical study of ultra-broadband wide-angle absorber," *Results Phys.*, vol. 24, 2021, Art. no. 104146.

[59] R. M. H. Bilal, S. Zakir, M. A. Naveed, M. Zubair, M. Q. Mehmood, and Y. Massoud, "Nanoengineered nickel-based ultrathin metamaterial absorber for the visible and short-infrared spectrum," *Opt. Mater. Exp.*, vol. 13, no. 1, pp. 28–40, 2023.

[60] D. Wu, L. Lei, M. Xie, P. Xu, and S. Xu, "High-performance metamaterial light absorption from visible to near-infrared assisted by anti-reflection coating," *Photonics*, vol. 10, no. 9, 2023, Art. no. 998.

[61] M. S. Raeen, A. Nella, and R. Maheswar, "A fourfold star petal–shaped polarization-insensitive broadband plasmonic metamaterial absorber," *Plasmonics*, vol. 18, no. 3, pp. 1059–1074, 2023.

[62] I. L. G. de Souza and V. F. Rodriguez-Esquerre, "Omnidirectional broadband absorber for visible light based on a modulated plasmonic multistack grating," *Opt. Laser Technol.*, vol. 124, 2020, Art. no. 105981.

[63] M. A. Naveed, R. M. H. Bilal, M. A. Baqir, M. M. Bashir, M. M. Ali, and A. A. Rahim, "Ultrawideband fractal metamaterial absorber made of nickel operating in the UV to IR spectrum," *Opt. Exp.*, vol. 29, no. 26, pp. 42911–42923, 2021.

[64] W. Cao, H. -D. Chen, Y. -W. Yu, N. Li, and W. -Q. Chen, "Changing profiles of cancer burden worldwide and in China: A secondary analysis of the global cancer statistics 2020," *Chin. Med. J.*, vol. 134, no. 07, pp. 783–791, 2021.
[65] M. Entezari et al., "Long non-coding RNAs and exosomal lncRNAs: Potential functions in lung cancer progression, drug resistance and tumor microenvironment remodeling," *Biomed. Pharmacother.*, vol. 150, 2022, Art. no. 112963.
[66] M. D. A. Paskeh et al., "Emerging role of exosomes in cancer progression and tumor microenvironment remodeling," *J. hematol. Oncol.*, vol. 15, no. 1, 2022, Art. no. 83.
[67] N. A. Hanjani et al., "Emerging role of exosomes as biomarkers in cancer treatment and diagnosis," *Crit. Rev. Oncol./Hematol.*, vol. 169, 2022, Art. no. 103565.
[68] Q. Maqsood, A. Sumrin, Y. Saleem, A. Wajid, and M. Mahnoor, "Exosomes in cancer: Diagnostic and therapeutic applications," *Clin. Med. Insights: Oncol.*, vol. 18, 2024, Art. no. 11795549231215966.
[69] Y. Van Der Pol and F. Mouliere, "Toward the early detection of cancer by decoding the epigenetic and environmental fingerprints of cell-free DNA," *Cancer Cell*, vol. 36, no. 4, pp. 350–368, 2019.
[70] F. Arshad, F. Nabi, S. Iqbal, and R. H. Khan, "Applications of graphene-based electrochemical and optical biosensors in early detection of cancer biomarkers," *Colloids Surfaces B: Biointerfaces*, vol. 212, 2022, Art. no. 112356.
[71] X. Chen et al., "Non-invasive early detection of cancer four years before conventional diagnosis using a blood test," *Nature Commun.*, vol. 11, no. 1, pp. 1–10, 2020.
[72] N. Pashayan and P. D. Pharoah, "The challenge of early detection in cancer," *Science*, vol. 368, no. 6491, pp. 589–590, 2020.
[73] D. M. Mittleman, "Twenty years of terahertz imaging," *Opt. Exp.*, vol. 26, no. 8, pp. 9417–9431, 2018.
[74] S. V. Gaponenko, *Introduction to Nanophotonics*. Cambridge, MA, USA: Cambridge Univ. Press, 2010.
[75] Q. Chen, X. Hu, L. Wen, Y. Yu, and D. R. Cumming, "Nanophotonic image sensors," *Small*, vol. 12, no. 36, pp. 4922–4935, 2016.
[76] K. W. Mauser et al., "Resonant thermoelectric nanophotonics," *Nature Nanotechnol.*, vol. 12, no. 8, pp. 770–775, 2017.
[77] C. Simovski and S. Tretyakov, *An Introduction to Metamaterials and Nanophotonics*. Cambridge, MA, USA: Cambridge Univ. Press, 2020.
[78] A. Kuzin et al., "Real-time surface functionalization of a nanophotonic sensor for liquid biopsy," *Appl. Phys. Lett.*, vol. 123, no. 19, 2023, Art. no. 193702.
[79] J. Zhang, L. Zhang, and W. Xu, "Surface plasmon polaritons: Physics and applications," *J. Phys. D: Appl. Phys.*, vol. 45, no. 11, 2012, Art. no. 113001.
[80] S. Im, S. Mousavi, Y. -S. Chen, and Y. Zhao, "Perspectives of chiral nanophotonics: From mechanisms to biomedical applications," *NPJ Nanophotonics*, vol. 1, no. 1, pp. 1–20, 2024.
[81] W. Bogaerts et al., "Silicon microring resonators," *Laser Photon. Rev.*, vol. 6, no. 1, pp. 47–73, 2012.